Effect of Pr^{3+} substitution on the microstructure, specific surface area, magnetic properties and specific heating rate of $Ni_{0.5}Zn_{0.5}\,Pr_xFe_{2-x}O_4$ nanoparticles synthesized via sol-gel method

Bing Yan[1], Peng-zhao Gao[1], Zhou-li Lu[1], Rui-Xue Ma[1], Evgeny V Rebrov[2,3], Hang-bo Zheng[1], Ying-xia Gao

[1] College of Materials Science and Engineering, Hunan University, Changsha, 410082, China
[2] School of Engineering, University of Warwick, Coventry, CV4 7AL, UK
[3] School of Chemistry and Chemical Engineering, Queen's University Belfast, Belfast BT9 5AG, UK

Corresponding author: Peng-zhao Gao

Email: gaopengzhao7602@hnu.edu.cn   Tel: +86 731 88822269; Fax: +86 731 88823554. (Peng-zhao Gao)

Abstract: A series of Ni-Zn ferrite nanoparticles with a nominal composition of $Ni_{0.5}Zn_{0.5}Pr_x\,Fe_{2-x}O_4$ (x=0.000 - 0.100 with steps of 0.025) has been synthesized by a sol-gel method. The effect of composition and calcination temperature on the morphology, specific surface area, magnetic properties and specific heating rate has been studied. The Ni-Zn-Pr ferrites have a single spinel (NZF) phase at Pr loadings below 5 at%. A minor amount of an orthorhombic $PrFeO_3$ phase is present in the Ni-Zn-Pr ferrites at Pr loadings above 5 at%. At a Pr loading of 10 at%, the specific surface area increases six-fold as compared to that of the non-doped $Ni_{0.5}Zn_{0.5}Fe_2O_4$ sample. As the Pr loading increases, the saturation magnetization, remnant magnetization and coercivity increase and reach the maximum at $x = 0.05$ and then decrease. The maximum values of these parameters are 67.0 emu/g, 9.7 emu/g and 87.2Oe, respectively. Under radiofrequency field (frequency: 295 kHz, intensity: 500 Oe), the highest heating rate of 1.65 K/s was observed over the sample with $x = 0.025$ which is 2.5 times higher than that of $Ni_{0.5}Zn_{0.5}Fe_2O_4$.

Keywords: sol-gel method; Pr^{3+} substitution Ni-Zn ferrite; Magnetic properties; Radio frequency heating.

1. Introduction

Nanostructured spinel type ferrites are promising materials that could be used as susceptors of induction heating in catalytic chemical reactors due to their high Curie temperatures and moderate magnetic losses in the kHz range. Moreover, they can be employed as magnetic catalysts or catalyst supports which facilitate magnetic separation [1]. The use of nanostructured magnetic materials for radiofrequency heating (RF) and magnetic separation within a chemical reactor provides a novel process intensified platform for system integration [2]. In these applications, magnetic nanoparticles embedded into composite catalytic microparticles are used as susceptors of induction or microwave heating [3, 4]. RF heating provides efficient, fast and uniform heat transfer into catalyst [5, 6] and flowing fluid [7-10].

Spinel ferrites have the general molecular formula $(A^{2+})[B_2^{3+}]O_4{}^{2-}$, where A^{2+} and B^{3+} are the divalent and trivalent cations occupying tetrahedral (A) and octahedral (B) interstitial positions of the *fcc* lattice formed by $O_2{}^{2-}$ ions. The Curie temperature and magnetic properties of ferrite materials depend on the type of cations and their distribution between the two interstitial positions. The latter in turn depends, among others, on the sintering conditions and grain size [11, 12]. As the grain size of nanostructured ferrites is much smaller than the skin depth, their heating rate in the kHz range is considerably higher than that of the bulk ferrites. The heating rates can further be adjusted by changing chemical composition of magnetic nanoparticles during their synthesis.

In recent years, low-cost soft magnetic Ni–Zn ferrites have been used in high-frequency devices due to their high values of chemical stability, magnetization, permeability, and low power losses [13, 14]. Ni–Zn polycrystalline ferrites, with an inverse spinel structure formed by a close-packed face centered cubic (FCC) lattice, can be represented with the general formula $(Zn_xFe_{1-x})[Ni_{1-x}Fe_{1+x}]O_4$, where the Zn^{2+} ions occupy the interstitial tetrahedral (A) sites, the Ni^{2+} ions occupy the octahedral (B) sites [4], and the Fe^{3+} ions are distributed between the A and B sites.

The desired magnetic properties of soft ferrites can be tailored by controlling the type and the amounts of different substitutes [15, 16]. Until now, several studies have been carried out to make improvements on the microstructure and magnetic properties of rare earth substituted ferrites [17–22].

The rare earth doped ferrites have widely been applied in modern telecommunication and electronic devices [23, 24]. An improvement in the intrinsic magnetic properties of the ferrite is achieved by a partial substitution of the Fe ions by metal ions with much larger ionic radius as compared to that of the Fe ions. The improvement is largely associated with the increase of magnetocrystalline anisotropy [25] as well as coercivity and saturation magnetization [26] and the latter two parameters can be either isotropic or anisotropic depending on the variation in the f electron orbital contribution to magnetic interactions [27]. Rezlescu et al. [22] demonstrated that rare earth ions could drastically influence the physical properties of substituted ferrites due to their larger ionic radius. At low dopant loadings, the rare earth ions could replace the Fe^{3+} ions in the octahedral sites of Ni–Zn ferrites. As the magnetic properties of ferrites are dominated by the antiferromagnetic superexchange interaction between the adjacent Fe^{3+} ions, this substitution induces Re^{+3}-Fe^{+3} interactions and modifies the saturation magnetization and coercivity and therefore the heating rate, especially in the kHz range. However the magnetic properties of the rare earth doped Ni–Zn ferrites have not been yet investigated.

Previously the Ni-Zn ferrites have been prepared by co-precipitation, ball milling, spray pyrolysis, combustion synthesis, hydrothermal synthesis, and sol–gel methods [28–33]. As the microstructure and magnetic properties of these ferrite materials are rather sensitive to the preparation method, some of those methods are not commercially viable due to disadvantages such as complexity, long synthesis time, or impurity penetration. Sol–gel is a flexible technique to adjust the properties of material by optimizing synthesis parameters such as hydrolysis time, temperature, precursor concentration and pH of the medium. The advantages of the sol–gel process include high purity of the resulting materials, their chemical

homogeneity, and high degree of control over particle and grain size. Furthermore, the method can easily be scaled up to a large production scale which is crucial for the development of chemical processes involving RF heating [14].

In the present work, the effect of Pr^{3+} addition to the Ni-Zn ferrites ($Ni_{0.5}Zn_{0.5}Pr_x Fe_{2-x}O_4$, x=0.000 - 0.100 with steps of 0.025) on the microstructure, specific surface area, magnetic properties and specific heating rate under RF heating in the kHz range has been studied. These materials are designed to provide high heating rates in novel types of catalytic flow reactors operated under RF heating [9, 10].

2. Experimental

2.1. Synthesis of materials

Substituted Ni-Zn ferrites were prepared by the sol-gel method [14]. Iron (III) nitrate nonahydrate, nickel(II) nitrate hexahydrate, zinc(II) nitrate hexahydrate, praseodymium(III) nitrate hexahydrate, and citric acid, ethanol, and ammonia solution (all from Aldrich Co., ACS grade) were used for the preparation of the starting sol. The metal nitrates were dissolved in ethanol in required molar ratios to prepare solution A. Citric acid was dissolved in ethanol in a separate vessel to produce solution B. Then solution B was added into solution A. The resulting mixture was stirred for 4 h and then it was quantitatively titrated by an aqueous ammonia solution to a pH of 2. The obtained sol was stirred for 24 h then dried in an oven at 353 K to get a series of Ni-Zn ferrite dry gels with different Pr loadings. The dry gels were milled and then calcined at 853, 923, 993, 1073 and 1203 K to produce the corresponding ferrite samples. The heating rate during calcination was 2 K·min^{-1} from 293 to 673 K and 5 K·min^{-1} from 673 K to the desired temperature [14].

The Pr substituted Ni-Zn ferrites are labeled as P-X-CT, where index X designates the Pr loading in Ni-Zn ferrites multiplied by 1000 and index CT designates the calcination temperature in Kelvin. For example, when the Pr loading in the Ni-Zn-Pr ferrite is equal to 0.050 (or 5 at.%) and the sample is calcined

at 993 K, it will be referred to as P-50-993 hereafter.

2.2. Characterizations of materials

The phase composition of the obtained samples was determined using an *X*-ray diffractometer (X'Pert PRO) with nickel filtered Cu K_α radiation produced at 40 kV and 27.5 mA, at a scanning rate of 5° min⁻¹ and a step of 0.02°. The Scherrer equation is used to calculate the crystal size (*D,* nm*)* [34].

$$D = \frac{k\lambda}{B\cos\theta} \tag{1}$$

where *k* equals to 0.89；*B* represents the peak width at half-height, λ is the wavelength. The *d(311)* interplanar spacing was determined from the position of the (311) peak using the Bragg equation.

The microstructure was studied with a transmission electron microscope (Philips, Tecnan F20) operated at 20 *kV*. The specific surface area was determined by nitrogen adsorption at 77 K on a Micromeritics NOVA 1000E nitrogen adsorption apparatus. The magnetization curves were measured by a vibrating sample magnetometer (Princeton Measurements Corporation MicroMag 3900 VSM) equipped with a 2 Tesla electromagnet at several temperatures in the range from room temperature to 673 K. The saturation magnetization (M_s), remnant magnetization (M_r), coercivity (H_c) and hysteresis losses were evaluated from the magnetization curves. Curie temperature (*T*c) was determined from the temperature dependence of magnetic moment measured with an applied magnetic field of 1.5 T in the 373-773 K range.

The specific heating rates were measured at a frequency of 295 kHz. The sample was placed in a quartz tube inserted along the center axis in a 50 mm RF coil connected to an Easy Heat RF system (Ambrell) operated at a current of 200 A. Prior to the measurements, a slurry of ferrite (10mg) in deionized water (80 mg) was made to enhance heat transfer towards the temperature sensor. The slurry temperature was measured with a fiber optic sensor (FISO). The specific heating rate was calculated from the initial (linear) part of temperature vs time curves taken into account the specific heat capacities of the ferrite and water in the slurry and their weight fractions.

3. Results and discussion

3.1 Effect of Pr loading on the composition, microstructure and magnetic properties of $Ni_{0.5}Zn_{0.5}Pr_x Fe_{2-x}O_4$ nanoparticles

3.1.1 Phase identification of $Ni_{0.5}Zn_{0.5}Pr_x Fe_{2-x}O_4$ nanoparticles with different Pr loadings

According to our previous study [14], $Ni_{0.5}Zn_{0.5}Fe_2O_4$ calcined at 1073K shows the highest specific heating rate, therefore this calcination temperature was chosen for further modifications. The XRD spectra of $Ni_{0.5}Zn_{0.5}Pr_x Fe_{2-x}O_4$ ferrites with different Pr loadings are shown in Figure 1. It can be seen that all peaks can be assigned to a $Ni_{0.5}Zn_{0.5}Fe_2O_4$ (NZF) spinel structure when the Pr loading is below 5 at%. This is in line with the results reported by Shirsath et al. [35]. However, when the Pr loading exceeds 5 at%, minor amounts of an orthorhombic $PrFeO_3$ phase are also present in the samples of the substituted ferrites in addition to major amounts of the $Ni_{0.5}Zn_{0.5}Fe_2O_4$ phase. Similar results were reported by Peng et al. [13]. As the Pr loading increases, the intensity of the $PrFeO_3$ peaks increases, confirming the higher amount of the $PrFeO_3$ phase in the doped samples. It can be seen from Figure 1b that the (311) peak first shifts to lower 2-theta values and then it shifts back to higher values. It means that the (311) interplanar spacing first increases and then decreases with the increase of Pr loading.

The average crystallite size, the (311) interplanar spacing and the lattice constant of the samples are listed in Table 1. The average crystal size decreases monotonously and it reaches the lowest value of 30.7 nm at a Pr loading of 0.100. It appears the Pr^{3+} ions reduce the degree of crystallinity and lower the crystal size of the Ni-Zn ferrite. These findings are in line with results reported by Huang et al. [36]. The binding energy of $Pr^{3+}-O^{2-}$ is bigger than that of $Fe^{3+}-O^{2-}$ [28], therefore more enthalpy is required to form the $Pr^{3+}-O^{2-}$ bond during crystal growth. This results in a smaller particles size in the Pr substituted ferrites. The

formation of the orthorhombic $PrFeO_3$ at the crystal boundaries further hinders the crystal growth in the

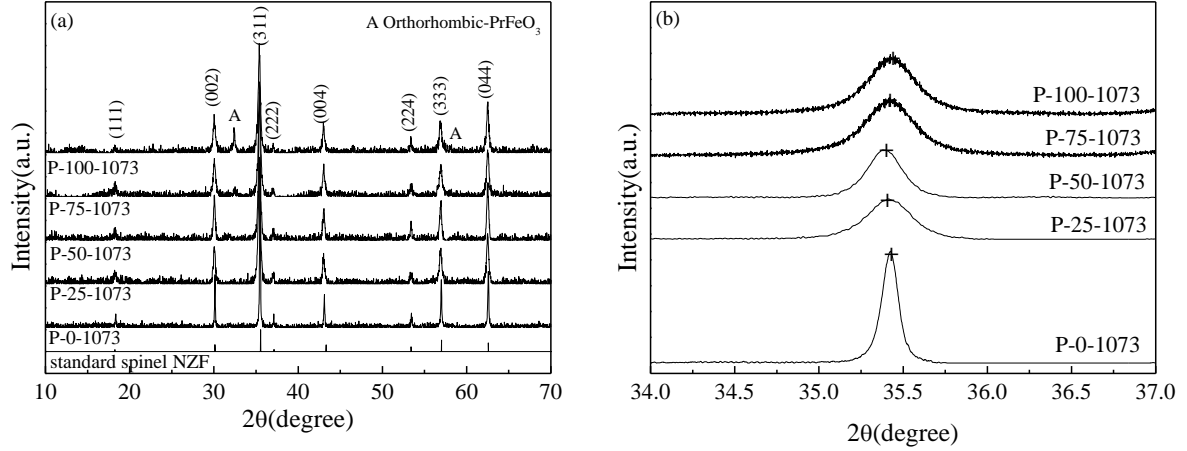Pr substituted ferrites.

Please insert Figure 1 here.

Figure 1. XRD patterns of $Ni_{0.5}Zn_{0.5}Pr_xFe_{2-x}O_4$ nanoparticles (x=0, 0.025, 0.05, 0.075, 0.1) calcined at 1073 K.

With the addition of Pr^{3+} ions, the lattice constant initially increases from 8.3768 Å in the pure Ni-Zn

ferrite to 8.3968 Å at a Pr loading of 0.05 and then decreases. The (311) interplanar spacing exhibits a

similar trend. These data can be explained based on the metal ion radius. According to Peng et al. [13],

the radius of Pr^{3+} ion of 1.13Å is larger than that of Fe^{3+} ion (0.67Å). The former occupies octahedral B

sites, similar to other ions from the lanthanide series. This replacement causes the expansion of unit cell,

resulting in larger lattice constants and interplanar spacing (Table 1). As the amount of the Pr dopant

increases, the Pr^{3+} ions could not enter the octahedral sites [13, 37]. As a result, the $PrFeO_3$ phase is formed,

thereby causing the overall lattice contraction.

Please insert Table 1 here.

Table 1 Physical properties of $Ni_{0.5}Zn_{0.5}Pr_xFe_{2-x}O_4$ nanoparticles (x=0, 0.025, 0.05, 0.075, 0.1)

Samples	P-0-1073	P-25-1073	P-50-1073	P-75-1073	P-100-1073
d_{311} interplanar spacing (nm)	2.5331	2.5387	2.5388	2.5378	2.5330
Lattice constant (Å)	8.3768	8.3940	8.3968	8.3834	8.3750
Average crystal size (nm) [a]	98.2	39.3	36.8	33.1	30.7
Specific surface area (m^2/g) [b]	5.9	36.0	36.0	37.0	37.0

Standard d_{311} interplanar spacing of $Ni_{0.5}Zn_{0.5}Fe_2O_4$ is 2.5330 nm and Lattice constant of it is 8.3830 Å

[a] Estimated error : ± 2%;   [b] Estimated error : ± 1%;

The grain size of the Pr-doped ferrites decreases with the addition of larger amounts of Pr ions (Table 1). Rezlescu et al. [22] suggested that due to the larger bond energy of $Pr^{3+}–O^{2-}$ as compared to that of $Fe^{3+}–O^{2-}$, more energy is needed to force the Pr^{3+} ions enter into the lattices and to form the bond of $Pr^{3+}–O^{2-}$. Therefore, the Pr^{3+}-substituted ferrites have higher thermal stability than the pure Ni–Zn ferrites, and more energy is needed for the substituted samples to complete grain crystallization and growth. According to Peng et al. [13], the formed $PrFeO_3$ phase is located near the grain boundary which in turn hinders the growth of ferrite grains. This explains the decrease in grain size with increasing the doping amount of Pr ions.

Specific surface area is an important parameter for catalytic applications of these materials. While the grain size decreases with the Pr loading, this does not change the specific surface area of these samples: the specific surface area of the Pr-doped ferrites increases six-fold as compared to that of the Ni-Zn ferrite and then remains virtually the same (Table 1). This could be due to the fact that the $PrFeO_3$ phase located near the grain boundaries can hinder the highly dispersed Ni-Zn ferrite nanoparticles for nitrogen adsorption, especially at larger Pr loadings. Therefore no increase in the surface area is observed even the size of individual ferrite nanoparticles decreases.

3.1.2 Microstructure of $Ni_{0.5}Zn_{0.5}Pr_x Fe_{2-x}O_4$ nanoparticles

TEM images of $Ni_{0.5}Zn_{0.5}Pr_x Fe_{2-x}O_4$ ferrites are shown in Figure 2. The $Ni_{0.5}Zn_{0.5}Fe_2O_4$ sample (Fig. 2a) consist of larger inter grown spherical particles with the mean size in the range between 100 and 140 nm, which is bigger than the average crystal size obtained from the XRD measurements. This difference could be explained by the fact that the resulting nanoparticles consist of several smaller crystallites. ~~While~~ The Pr-doped ferrite nanoparticles (see Fig. 2b - 2e) consist of irregular hexagon and oval polyhedrons with the mean size between 50 and 100 nm. Their smaller size is due to partially suppressed aggregation as a result of repulsive molecular forces between the individual nanocrystallites [14]. In this case, the particle size also seems to be bigger than the crystallite size obtained from the XRD spectra. This is due to the formation of connecting necks between the two neighboring particles during sintering process. As compared with the Ni-Zn ferrite (Fig. 2a), the doped nanoparticles exhibit much better dispersion. It can be seen that only a few particles severely agglomerate, while most of them are interconnected to form thread-liked structures that also help to improve the specific surface area of the Pr-doped Ni-Zn ferrites.
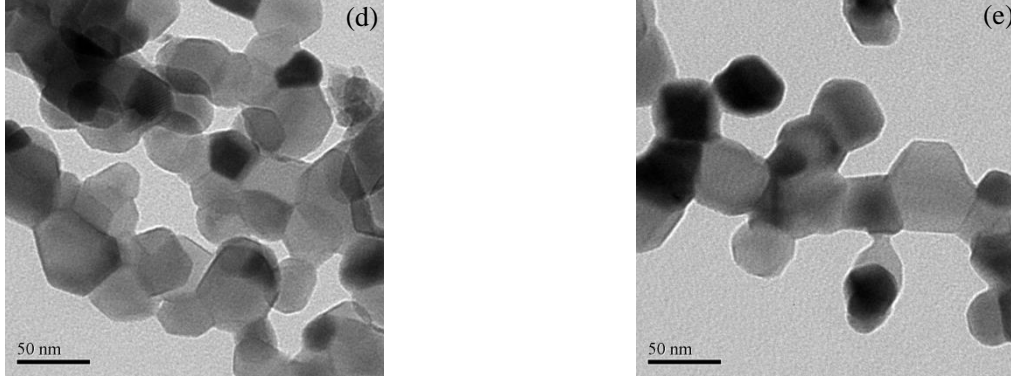
Please insert Figure 2 here.

(a)

(b)

(c)

100 nm

100 nm

50 nm
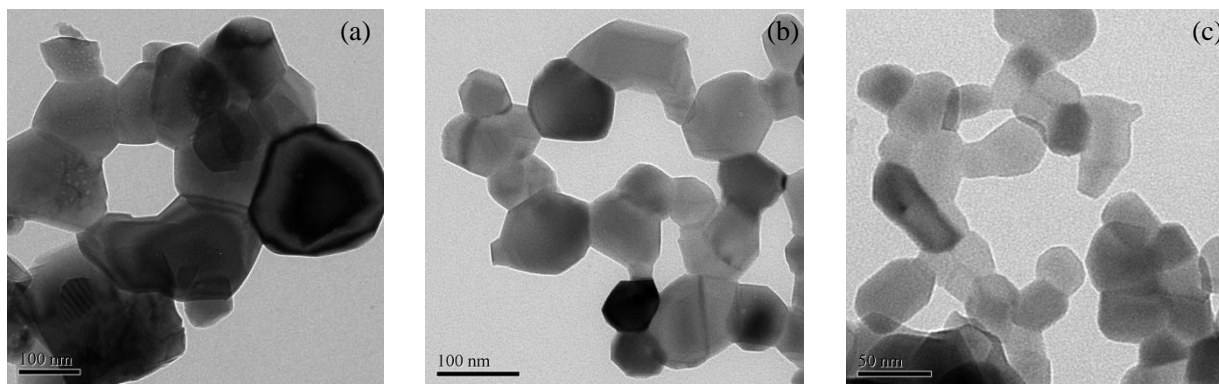
Figure 2. TEM images of $Ni_{0.5}Zn_{0.5}Pr_xFe_{2-x}O_4$ nanoparticles (a) P-0-1073 (b), P-25-1073, (c) P-50-1073, (d) P-75-1073, (e) P-100-1073.

3.1.3 Magnetic properties of $Ni_{0.5}Zn_{0.5}Pr_x Fe_{2-x}O_4$ nanoparticles

The magnetization curves of Pr-doped Ni-Zn ferrites samples are shown in Figure 3. Figure 4a shows the values of saturation and remnant magnetization, while the coercivity and Curie temperature are shown in Figure 4b as a function of Pr loading.
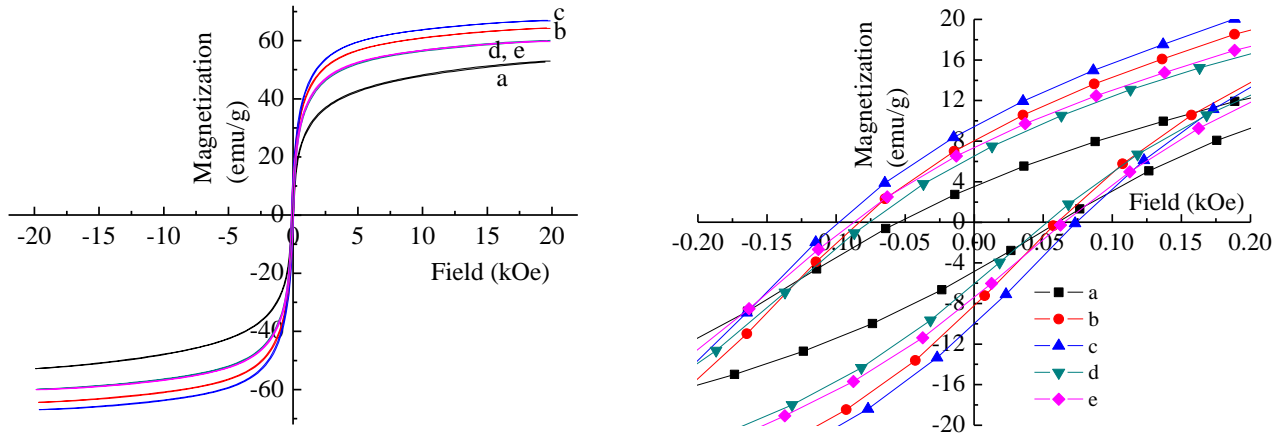
Please insert Figures 3 and 4 here.

Figure 3. Magnetization curves of (a) P-0-1073, (b) P-25-1073, (c) P-50-1073, (d) P-75-1073, (e) P-100-1073.
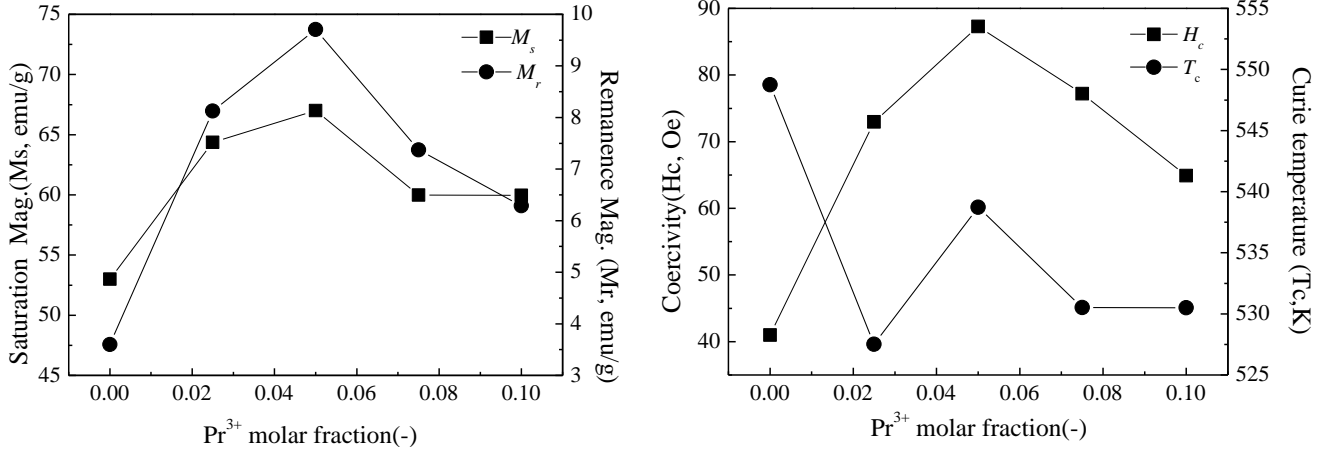
Figure 4.   (a) Saturation and remnant magnetization, (b) coercivity and Curie temperature of $Ni_{0.5}Zn_{0.5}Pr_xFe_{2-x}O_4$ as a function of Pr loading.

As the Pr loading increases, the saturation magnetization, remnant magnetization and coercivity increase and reach the maximum at x = 0.05 and then decrease (Fig.4a and b). The maximum values of these parameters are 67.0 emu/g, 9.7 emu/g and 87.2Oe, respectively. The observed trends for M_s and M_r can be explained by the amount and distribution of Pr^{3+} in the Ni-Zn ferrite lattice. According to Shinde et al. [38], the Zn^{2+} and partially Fe^{3+} ions occupy the A sites while the Ni^{2+} and the remaining Fe^{3+} ions occupy the B sites of Ni-Zn ferrite: $(Zn_x^{2+}Fe_{1-x}^{3+})^A (Ni_{1-x}^{2+}Fe_{1+x}^{3+})^B$. The dependence of M_s on composition can be estimated with Eq. 2.

$$M_{total} = M_B - M_A = \mu_{B,Ni} + \mu_{B, Fe} + \mu_{B, Pr} - \mu_{A,Fe} - \mu_{A,Zn} \tag{2}$$

where μ_i is the magnetic moment of the corresponding ions. Their values are reported in Ref [36].

When the Pr loading is below 5 at.%, the Pr^{3+} ions occupy the B-sites only [13] and the Fe^{3+} ions remain in the spinel structure as confirmed by the XRD data. Pachpinde et al. [25] have shown that the number of Ni ions displaced from the B-sites to the A-sites increases when the Pr^{3+} loading increases. This leads to an increase of the net magnetic moment because the magnetic moment of the B-lattice, M_B, increases faster as compared to that of M_A [25]. This is due to a slightly higher magnetic moment of the Pr^{3+} ion of

11

3.61 as compared to that of the Ni^{2+} ion of 3.50 [36]. However when the Pr loading exceeds 5 at.%, an excess of Pr^{3+} ions causes the formation of a new $PrFeO_3$ phase when reacting with the Fe^{3+} ions that moved out from the B-sites decreasing M_B. This decreases the overall magnetic moment and saturation magnetization.

According to Boys and Legvold [39], Nellis and Legvold [40] and Zhou et al. [41], the $4f$ electrons of rare earths elements (Re) generally remain highly localized in the solid and form the magnetic electrons. In this way, they are screened from the crystal field by the $5d$ and $6s$ electrons and therefore they cannot have strong magnetic interactions with neighbor cations in the rare earths elements. This leads to the decrease in the negative exchange interactions between Re^{3+} and Fe^{3+} ($4f - 3d$ coupling). Therefore the $Re^{3+}- Fe^{3+}$ and $Re^{3+}-Re^{3+}$ (indirect $4f - 5d - 4f$ electrons coupling) interactions are rather weak [42].

As the Pr loading increases, the coercivity of Pr substituted Ni-Zn ferrites first increases and then decreases (Figure 4b). At the Pr loading below 5 at.%, the coercivity of the ferrites depends inversely on the grain size [43]. Above the 5 at% Pr loading, the formation of $PrFeO_3$ phase decreases the number of domain rotation contributions to magnetization, which lowers the coercivity.

The Curie temperature of the substituted Ni-Zn ferrites is in the range between 528 and 549 K which is in line with the data presented by Peng et al. [13] (Figure 4b). Curie temperature depends on the A–B exchange interaction, which is the strongest one among the three A–A, B–B and A–B interactions, in which the interaction between Fe^{3+} ions plays a leading role [44]. Compared with the $Ni_{0.5}Zn_{0.5}Fe_2O_4$ sample, the substitution of Fe^{3+} with Pr^{3+} decreases the net magnetic moment and the exchange interaction between the A and B sublattices, decreasing the Curie temperature. As the Pr loading increases, a slight fluctuation of Curie temperature is observed, being a result of a non-uniform distribution of the Pr^{3+} and Fe^{3+} ions in the two sublattices.

The highest saturation magnetization was observed in the Pr-doped sample with a Pr loading of 5 at%. Therefore this sample was chosen to investigate the effect of calcination temperature.

3.2 Effect of calcination temperature on the microstructure and magnetic properties

Figure 5 shows XRD spectra of $Ni_{0.5}Zn_{0.5}Pr_{0.05}Fe_{1.95}O_4$ samples calcined at different temperatures. The sample calcined at 853 K has amorphous structure. The formation of spinel phase was observed in the 923-1203 K range. The average crystallite size, interplanar spacing, and specific surface area of $Ni_{0.5}Zn_{0.5}Pr_{0.05}Fe_{1.95}O_4$ nanoparticles are listed in Table 2. It can be seen that the surface area decreases by a factor of 4 as the calcination temperature increases from 853 to 1203 K due to progressive aggregation of small crystallites into larger particles.
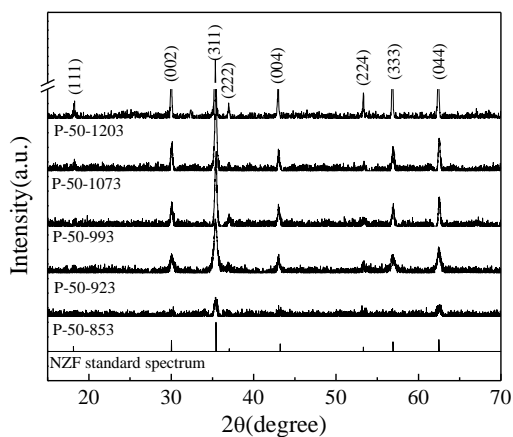
Please insert Figure 5 here.

Figure 5. XRD spectra of $Ni_{0.5}Zn_{0.5}Pr_{0.05}Fe_{1.95}O_4$ nanoparticles calcined at different temperatures.

Please insert Table 2 here.

Table 2 Physical and magnetic properties of $Ni_{0.5}Zn_{0.5}Pr_{0.05}Fe_{1.95}O_4$ nanoparticles calcined at different temperatures

Sample	P-50-853	P-50-923	P-50-993	P-50-1073	P-50-1203
Average crystal size (nm) [a]	A	24.1	32.8	33.1	91.1
(311) interplanar spacing (nm)	A	2.5374	2.5388	2.5402	2.5411
Specific surface area (m^2/g) [b]	49	41	38	36	13
Saturation magnetization (emu/g)[c]	41.1	54.8	63.1	67.0	74.1
Remnant magnetization (emu/g)[d]	1.0	4.3	7.9	9.7	6.9
Coercivity (Oe) [e]	19.5	58.8	85.4	87.3	37.6
Curie temperature (K) [f]	-	529	534	539	543

A - Amorphous

[a] Estimated error : ± 2%; [b] Estimated error : ± 1%; [c, d and e] Estimated error : ± 1%; [f] Estimated error : ±0.5 %.

TEM images of $Ni_{0.5}Zn_{0.5}Pr_{0.05}Fe_{1.95}O_4$ nanoparticles calcined at different temperatures are shown in Figure 6. The particles form irregular polyhedrons with mean sizes between 20 and 120 nm connected by necks. The magnetic attraction force is responsible for agglomeration of particles and results in this specific shape after calcination. As the calcination temperature increases, the amount of amorphous phase decreases and the particle size increases.

Please insert Figure 6 here

(a) (b) (c)

(d) (e)

14

Figure 6. TEM images of $Ni_{0.5}Zn_{0.5}Pr_{0.5}Fe_{1.95}O_4$ nanoparticles calcined at different temperatures.(a) P-50-853, (b) P-50-923, (c) P-50-993, (d) P-50-1073, (e) P-50-1203.

Magnetic properties of $Ni_{0.5}Zn_{0.5}Pr_{0.05}Fe_{1.95}O_4$ nanoparticles calcined at different temperatures are shown in Figure 4. It can be se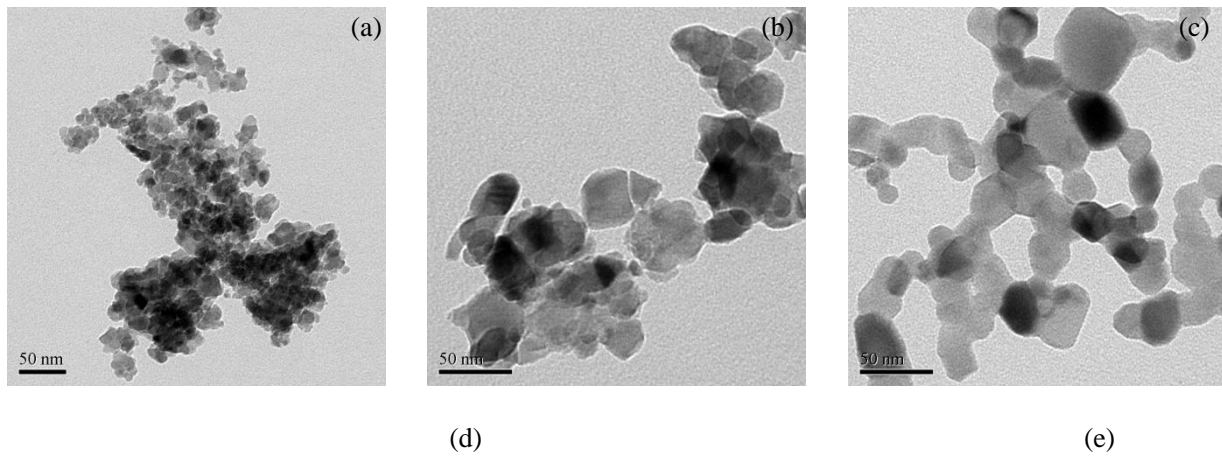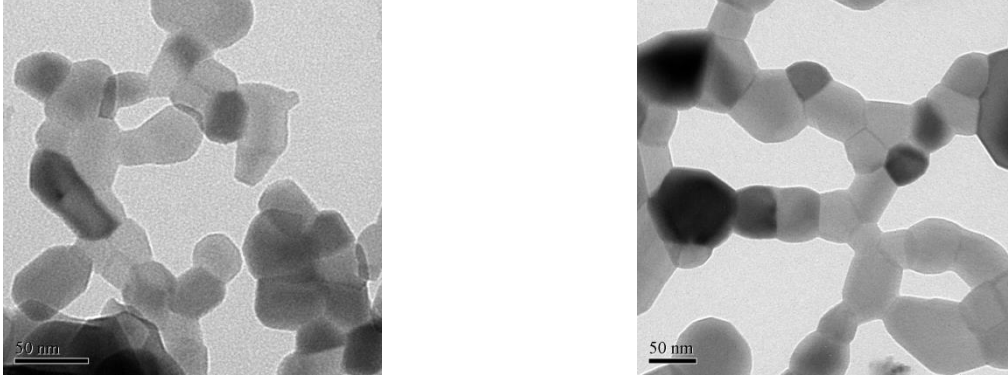en that as the calcination temperatures increases from 853 to 1203 K, the saturation magnetization and Curie temperature increase. The saturation magnetization is influenced by intrinsic factors such as preferential site occupancy of the cations, composition as well as by extrinsic factors like microstructure and bulk density of the ferrites [45]. The saturation magnetization monotonously increases with calcination temperatures and reaches the maximum value of 74.1 emu/g (Table 2). This effect is related to larger grain size in P-50-1203. The maximum value exceeds that of the bulk Ni-Zn ferrite (56 emu/g) [46]. The observed dependence is a combined effect of increased grain size and the increased exchange interaction in the material with densely packed grains [47].

The highest coercivity of 87.3 Oe is observed in P-50-1073 as this sample has the grain size close to transition size from single to multidomain region (Table 2). The critical grain size (d_{cr}) was estimated by Eq. 3 [48]:

$$d_{cr} = \frac{9\varepsilon_p}{2\pi M_s^2} \qquad \text{(in CGS units)} \tag{3}$$

where M_s is the saturation magnetization and ε_p is the surface energy of the domain wall:

$$\varepsilon_p = \left(\frac{2k_B T_C K_1}{a} \right)^{0.5} \tag{4}$$

where k_B is the Boltzmann constant (1.38×10^{-16} erg·K^{-1}), T_c the Curie temperature, a is the lattice parameter, and K_1 is the absolute value of magnetocrystalline anisotropy constant. It was reported that the anisotropy constant only slightly changes with composition [14, 48]. Therefore in these calculations, an assumption was made that K_1 remains constant and equal to that in the P-0-1073 sample. The obtained parameter values are listed in Table 3.

Please insert Table 3 here.

Table 3 Parameters used in estimation of critical grain size

Parameter	Value	Reference
T_c (K) [a]	539	This study
a (cm)	8.40×10^{-8}	This study
M_s (emu·g^{-1}) [b]	67.0	This study
K_1 (erg/cm^3)	1.5×10^{-4}	[14]
ε_p (erg/cm^2)	0.11	Eq. 4
d_{cr} (nm)	35	Eq. 3

[a] Estimated error : ± 0.5 %;   [b] Estimated error : ± 1%;   [c, d and e] Estimated error : ± 1%

Below the critical size of 35 nm, the coercivity increases with the increase in particle size and then decreases as the P-50-1203 sample has a multidomain structure (Table 2). As the calcination temperature increases, the Curie temperature of Ni$_{0.5}$Zn$_{0.5}$Pr$_{0.5}$Fe$_{1.95}$O$_4$ nano- particles increases from 528 to 543 K (Table 2). A similar trend was observed by Sepelak et al. [49] for nanoscaled Ni ferrites. These authors observed that Curie temperature increases from 849 to 858 K with increasing annealing temperature from 1018 to 1198 K due to the cation reequilibration process.

The temperature dependences of magnetic properties of P-50-1073 and P-0-1073 samples are shown in Figure 7. As the temperature increases, the saturation magnetization, remnant magnetization and coercivity monotonously decrease.

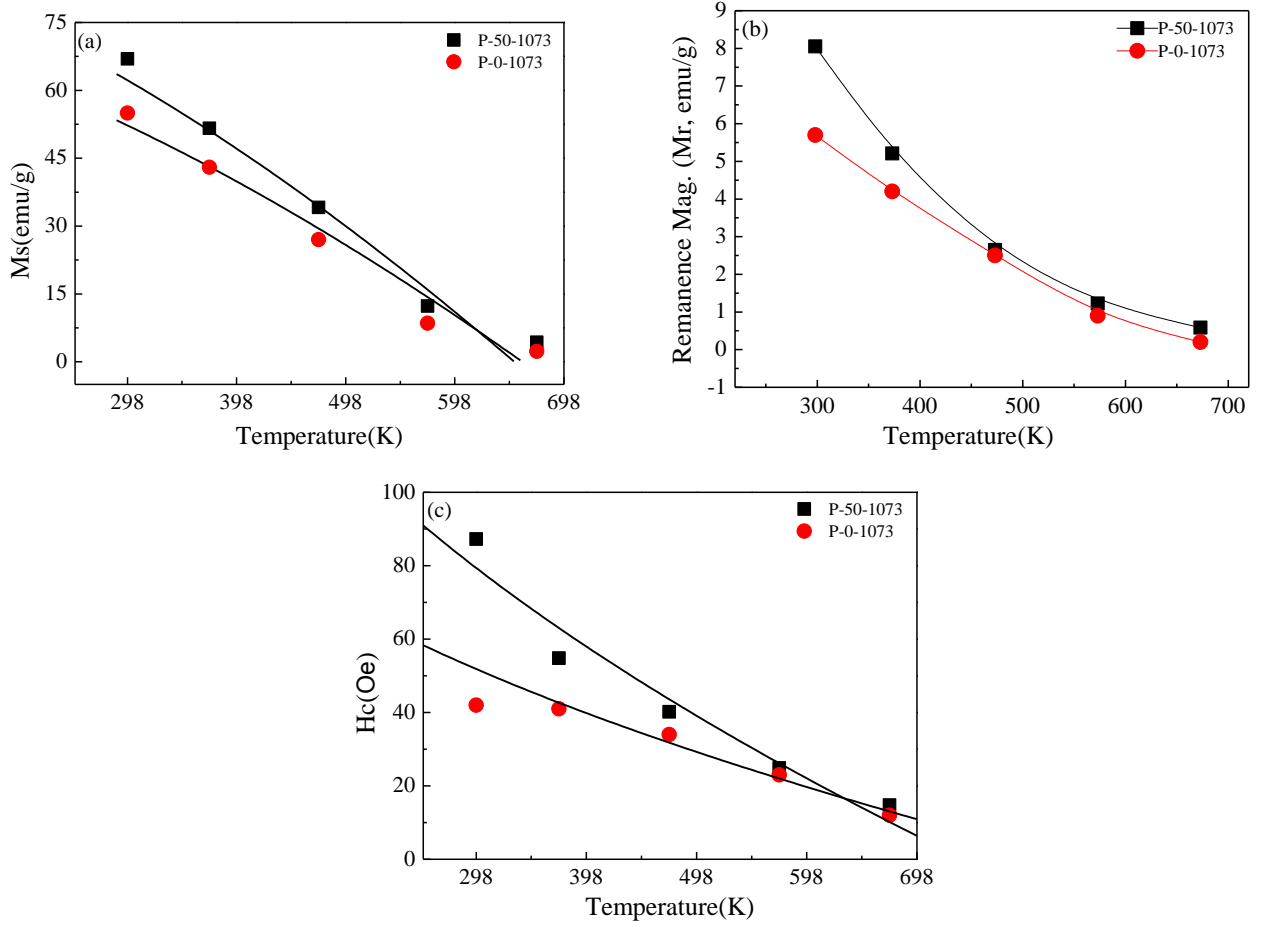Please insert Figure 7 here.

Figure 7. (a) Saturation magnetization, (b) remnant magnetization, (c) coercivity of P-50-1073 and P-0-1073 as a function of temperature. Symbols represent experimental data. Solid lines in (a) and (c) represent predictions by Eqs. 5 and 6, respectively; lines in (b) are guides for the eye.

The temperature dependence of saturation magnetization is described by Eq. 5 [50].

$$M_s = M_{S0}\,(1\text{-}BT^b) \tag{5}$$

where B is the Bloch constant, M_{S0} is the saturation magnetization at $T = 0$ K, and b is the Bloch exponent. For nanostructured materials, Mills and Maradudin reported the Bloch exponent of 1.5, as for bulk

materials [51]. The Bloch exponent b may increase as the particle size decreases [52]. Zhang et al. reported b in the range 1.5–2.0 for $MnFe_2O_4$ nanoparticles with sizes in the range 5-15 nm [53]. However, our results obtained by fitting experimental data using Eq. 5, show that the Bloch constant of the Pr-substituted Ni-Zn ferrite does not depend on the particle size (Table 4).

Coercivity decreases with an increase in temperature according to Eq. 6 [54]:

$$H_c = H_{c0}\left(1 - \sqrt{\frac{T}{T_B}}\right) \tag{6}$$

where H_{c0} is the coercivity at $T = 0$ K and T_B is the blocking temperature below which hysteresis appears. The corresponding parameters are listed in Table 4.

Table 4 Fitting parameters for the temperature dependence of M_s and H_c according to Eqs. 5, 6

Sample	M_{SO} (emu/g)[a]	B (K^{-b})	b (-)[b]	H_{CO} (G)[c]	T_B (K)
P-0-1073	74.9	5.9×10^{-5}	1.5	129	833
P-50-1073	90.0	5.8×10^{-5}	1.5	217	741

[a] Estimated error : ± 1 %; [b] Estimated error : ± 1%; [c and d] Estimated error : ± 1%

3.3 Hysteresis loss and specific heating rate

Hysteresis loss (P) is an important factor in evaluating the performance of materials intended for RF heating [9, 10]. The hysteresis loss is proportional to the area between the two magnetization curves. In our previous work, we suggested a simple relation between the hysteresis loss, coercivity and saturation magnetization [14]:

$$P = C_0 \cdot H_c \cdot M_s \tag{7}$$

Where C_0 is a constant, which shows the ratio of the actual hysteresis loss to that in the case in which the magnetization curves form a rectangle with edges of M_S and H_c. Hysteresis loss of P-0-1073 and P-50-1073 as a function of temperature are shown in Figure 8.
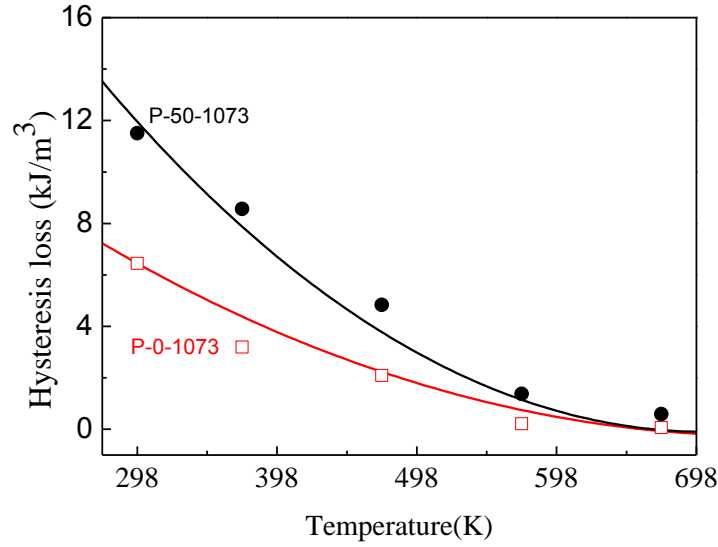
Please insert Figure 8 here.

Figure 8. Hysteresis loss of P-0-1073 and P-50-1073 as a function of temperature.
Symbols represent experimental data. Solid lines represent predictions by Eq. 7.

It can be seen that a good agreement is obtained between the predicted and experimental values in the whole range of temperature data. Therefore, the higher the saturation magnetization, the more heat is produced/cycle of the magnetization reversal process. However, the latter is only true if the field magnitude is higher than the coercivity [2]. Therefore, although these magnetic materials could theoretically produce more heat, in practice there are technical restrictions imposed on the amplitude of the applied field. In this study, the amplitude of magnetic field inside the coil was limited to 500 Oe. Therefore, the heating rate is proportional to the actual hysteresis loss inside the coil. The latter is proportional to the area enclosed between the two magnetization curves and two vertical lines corresponding to magnetic field intensity of - 500 and 500 Oe. The heating rate is shown in Figure 9 as a function of the actual hysteresis loss in the coil.
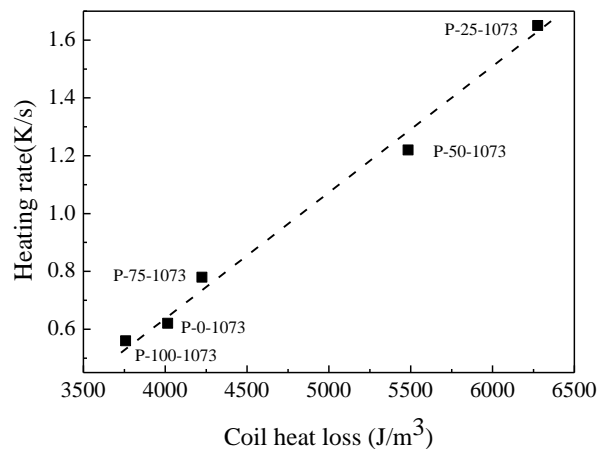
Figure 9. Heating rate of nickel zinc ferrites samples as a function of coil heat loss.

The sample P-25-1073 exhibits the highest heating rate of 1.65 K/s, which is 2.5 times higher than that of pure nickel zinc ferrite (P-0-1073). It should be mentioned that while P-50-1073 has a higher value of saturation magnetization as compared to that of P-25-1073, the remnant magnetization values of these samples are rather close to each other. The remnant magnetization determines the shape of magnetization curves in weak magnetic fields. As the coercivity of these samples is much higher than the magnetic field produced by the test coil, the sample with lower coercivity produce higher hysteresis loss in weak RF field. Thus while P-50-1073 has a potential to provide higher heating rate in a strong RF field (above 1 kOe), the performance of P-25-1073 is much better in terms of heating rate in a relatively weak magnetic field of 500 Oe.

4. Conclusions

A series of Ni-Zn ferrite nanoparticles with a nominal composition $Ni_{0.5}Zn_{0.5}Pr_x Fe_{2-x}O_4$ (x=0.000 - 0.100 with steps of 0.025) were prepared by a sol-gel method. The effect of composition and calcination temperature on the morphology, specific surface area, magnetic properties and specific heating rate under radiofrequency heating was studied. The Pr^{3+} addition to the Ni-Zn ferrite lattice drastically reduces the

average crystal size and results in a six-fold increase of specific surface area of the resulting materials. Below Pr/Ni molar ratios of 0.1, the cubic ferrite spinel is the only phase present. At higher Pr loadings, the formation of an orthorhombic $PrFeO_3$ phase takes place. As the Pr^{3+} loading increases, the saturation magnetization, remnant magnetization and coercivity increase, reach the maximum at a Pr loading of 5 at% and then decrease. The maximum values of these parameters are 67.0 emu/g, 9.7 emu/g and 87.3 Oe, respectively. The doped sample with a Pr loading of 2.5 at% calcined at 1073 K demonstrated the highest specific heating rate of 1.65K /s in a weak RF field of 500 Oe at a frequency of 295 kHz. This heating rate 2.5 times exceeds that observed over the non-doped nickel zinc ferrite under the same operating conditions.

5. Acknowledgements

References

[1] R. Benraba, H. Boukhlouf, A. Löfberg, A. Rubbens, R.-N. Vannier, E. Bordes, R.A. Barama. Nickel ferrite spinel as catalyst precursor in the dry reforming of methane: synthesis, characterization and catalytic properties. *J Nat Gas Chem* 2012; **21**: 595–604.

[2] T.K. Houlding, E.V. Rebrov. Application of alternative energy forms in catalytic reactor engineering. *Green Process Synth* 2012;**1**:19–32.

[3] E.V. Rebrov, P. Gao, T.M.W.G.M. Verhoeven, J.C. Schouten, R. Kleismit, Z. Turgut, G. Kozlowski. Structural and magnetic properties of sol–gel $Co_{2x}Ni_{0.5-x}Zn_{0.5-x}Fe_2O_4$ thin films. *J Magn Magn Mater* 2011; **323**: 723–729.

[4] P. Gao, E.V. Rebrov, T.M.W.G.M. Verhoeven, J.C. Schouten, R. Kleismit, G. Kozlowski, J. Cetnar, Z. Turgut, G. Subramanyam. Structural investigations and magnetic properties of sol–gel $Ni_{0.5}Zn_{0.5}Fe_2O_4$ thin films for microwave heating. *J Appl Phys* 2010; **107**: 044317:1-7.

[5] A. Ovenston, J.R. Walls, Generation of heat in a single catalyst pellet placed in an electromagneticfield for endothermic reforming of hydrocarbons. *J Chem. Soc Faraday Trans 1: Phys Chem Condens Phases* 1983; **79**: 1073–1084.

[6] S.I. Al-Mayman, S.M. Al-Zahrani, Catalytic cracking of gas oils in electromagneticfields: reactor design and performance. *Fuel Process Technol* 2003; **80**:169–182.

[7] P. Duquenne, A. Deltour, G. Lacoste. Application of inductive heating to granular media: temperature distribution in a granular bed. *Int J Heat Mass Transfer* 1993; **36**: 2473–2477.

[8] T.K. Houlding, K. Tchabanenko, M.T. Rahman, E.V. Rebrov, Direct amide formation using radiofrequency heating, *Org Biomol Chem* 2013; **11**: 4171–4177.

[9] S. Chatterjee, V. Degirmenci, F. Aiouache, E.V. Rebrov Design of a radio frequency heated isothermal micro-trickle bed reactor. *Chem Eng J* 2014; **243**: 225–233.

[10] T.K. Houlding, P. Gao, V. Degirmenci, K. Tchabanenko, E.V. Rebrov, Mechanochemical synthesis of $TiO_2/NiFe_2O_4$ magnetic catalysts for operation under RF field. *Mater Sci Eng B* 2014; in press http://dx.doi.org/10.1016/j.mseb.2014.12.011.

[11] C.N. Chinnasamy, A. Narayanasamy, N. Ponpandian, K. Chattopadhyay, K. Shinoda, B. Jeyadevan, K. Tohji, K. Nakatsuka, T. Furubayashi, I. Nakatani. Mixed spinel structure in nanocrystalline $NiFe_2O_4$. *Phys Rev B* 2001; **63**:184108:1-6 .

[12] L.D. Tung, V. Kolesnichenko, G. Caruntu, D. Caruntu, Y. Remond, V.O. Golub, C. J. O'Connor, L. Spinu. Annealing effects on the magnetic properties of nanocrystalline zinc ferrite. *J Phys: Condens Matter* 2002; **319**: 116–121.

[13] Z. Peng, X. Fu, H. Ge, Z. Fu, C. Wang, L. Qi, H. Miao. Effect of Pr^{3+} doping on magnetic and dielectric properties of Ni–Zn ferrites by one-step synthesis. *J Magn Magn Mater* 2011; **323**: 2513–2518.

[14] P. Gao, X. Hua, V. Degirmenci, D. Rooney, M. Khraisheh, R. Pollard, R.M. Bowman, E. V. Rebrov. Structural and magnetic properties of $Ni_{1-x}Zn_xFe_2O_4$ (x=0, 0.5 and 1) nanopowders prepared by sol–gel method. *J Magn Magn Mater* 2013; **48**: 44-50

[15] W.A.A. Bayoumy. Synthesis and characterization of nano-crystalline Zn-substituted Mg–Ni–Fe–Cr ferrites via surfactant-assisted route. *J Mol Struct* 2014; **1056–1057**: 285-291.

[16] A. Ghasemi, M. Mousavinia. Structural and magnetic evaluation of substituted $NiZnFe_2O_4$ particles synthesized by conventional sol–gel method. *Ceram Int* 2014; **40**: 2825-2834.

[17] R.C. Kambale, K.M. Song, C.J. Won, K.D. Lee, N. Hur. Magnetic and magnetostrictive behavior of Dy^{3+} doped $CoFe_2O_4$ single crystals grown by flux method. *J Cryst Growth* 2012; **340**: 171–174.

[18] J. Sahariy, H.S. Mund, A. Sharma, A. Dashora, M. Itouc, Y. Sakurai, B.L. Ahuja. Magnetic properties of $NiFe_{2-x}RE_xO_4$ (RE=Dy, Gd) using magnetic Compton scattering. *J Magn Magn Mater* 2014; **360**:113–117.

[19] E.E. Ateian, M.A. Ahmed, L.M. Salah, A.A. El-Gamal. Effect of rare earth oxides and La^{3+} ion concentration on some properties of Ni–Zn ferrites. *Phys B* 2014; **445**: 60–67.

[20] P. Samoila, T. Slatineanu, P. Postolache, A.R. Iordan, M.N. Palamaru. The effect of chelating / combustion agent on catalytic activity and magnetic properties of Dy doped Ni-Zn ferrite. *Mater Chem Phys* 2012; **136**: 241-246.

[21] S.S.R. Inbanathan, V. Vaithyanathan, J.A. Chelvane, G. Markandeyulu, K.K. Bharath. Mössbauer studies and enhanced electrical properties of R (R=Sm, Gd and Dy) doped Ni ferrite. *J Magn Magn Mater* 2014; **353**: 41–46.

[22] N. Rezlescu, E. Rezlescu, C. Pasnicu, M.L. Craus. Effects of the rare-earth ions on some properties of a nickel–zinc ferrite. *J Phys : Condens Matter* 1994; **6**: 5707–5716.

[23] Farhana Kousar, Sidra Nazim, Muhammad Farooq Warsi, Muhammad Azhar Khan, Muhammad Naeem Ashiq, Zaheer Abbas Gilani, Imran Shakir, Abdul Wadood. $La_{1-x}Eu_xFeOs_3$ nanoparticles: Fabrication via micro-emulsion route for high frequency devices applications**. *J Alloys Compd* 2015; **629**: 315-318.

[24] Shokat Nawaz, Huma Malik, Muhammad Farooq Warsi, Muhammad Shahid, Imran Shakir, Abdul Wadood, Muhammad Azhar Khan. New $La_{1-x}Cr_{0.7x}Eu_{0.3x}FeO_3$ nanoparticles: Synthesis via wet chemical route, structural characterization for magnetic and dielectric behavior evaluation. *Ceram Int* 2015; **41**: 6812-6816.

[25] A.M. Pachpinde, M.M. Langade, K.S. Lohar, S.M. Patange, Sagar E. Shirsath. Impact of larger rare earth Pr^{3+} ions on the physical properties of chemically derived $Pr_xCoFe_{2-x}O_4$ nanoparticles. *Chem Phys*. 2014; **429**: 20–26.

[26] Muhammad Waqas Mukhtar, Muhammad Irfan, Ishtiaq Ahmad, Ihsan Ali, Majid Niaz Akhtar, Muhammad Azhar Khan, Ghazanfar Abbas, M.U. Rana, Akbar Ali, Mukhtar Ahmad. Synthesis and properties of Pr-substituted MgZn ferrites for core materials and high frequency applications. *J Magn Magn Mater.* 2015, **381**: 173–178.

[27] Z. Karimi, Y. Mohammadifar, H. Shokrollahi, Sh. Khameneh Asl, Gh. Yousefi, L. Karimi. Magnetic and structural properties of nano sized Dy-doped cobalt ferrite synthesized by co-precipitation. *J Magn Magn Mater* 2014; **361**: 150–156.

[28] S.J. Azhagushanmugam, N. Suriyanarayanan, R. Jayaprakash. Synthesis and characterization of nanocrystalline $Ni_{(0.6)} Zn_{(0.4)} Fe_2O_4$ spinel ferrite magnetic material. *Phys Procedia*, 2013; **49**: 44-48

[29] Kh. Gheisari, Sh. Shahriari, S. Javadpour. Structure and magnetic properties of ball-mill prepared nanocrystalline Ni–Zn ferrite powders at elevated temperatures. *J Alloys Compd* 2013; **552**: 146-151.

[30] A. Sutka, G. Strikis, G. Mezinskis, A. Lusis, J. Zavickis, J. Kleperis, D. Jakovlevs. Properties of Ni–Zn ferrite thin films deposited using spray pyrolysis. *Thin Solid Films* 2012; **526**: 65-69.

[31] V.V. Awati, S.M. Rathod, Sagar E. Shirsath, Maheshkumar L. Mane. Fabrication of Cu^{2+} substituted nanocrystalline Ni–Zn ferrite by solution combustion route: Investigations on structure, cation occupancy and magnetic behavior. *J Alloys Compd* 2013; **553**:157-162.

[32 U. Wongpratat, S. Meansiri, E. Swatsitang. Local structure and magnetic property of $Ni_{1-x}Zn_xFe_2O_4$ (x = 0, 0.25, 0.50, 0.75, 1.00) nanoparticles prepared by hydrothermal method. *Microelectron Eng* 2014; **126**: 19-26.

[33] Y. Liu, J.-J. Li, F.-F. Min, J.-Bo Zhu, M.-X. Zhang. Microwave-assisted synthesis and magnetic properties of $Ni_{1-x}Zn_xFe_2O_4$ ferrite powder. *J Magn Magn Mater* 2014; **354**: 295-298.

[34] G. Herzer Grain size dependence of coercivity and permeability in nano-crystalline ferromagnet. *IEEE Trans Magn* 1990; **26**: 1397-1402.

[35] Sagar E. Shirsath, R.H. Kadam, Anil S. Gaikwad, Ali Ghasemi, Akimitsu Morisako. Effect of sintering temperature and the particle size on the structural and magnetic properties of nanocrystalline $Li_{0.5}Fe_{2.5}O_4$. *J Magn Magn Mater* 2011, 323: 3104–3108.

[36] B. Huang. Nanostructure magnetic cobalt ferrites [D]. China Jiliang University, 2012, p. 43

[37] E.E. Ateia, M.A. Ahmed, L.M. Salah, A.A. El-Gamal. Effect of rare earth oxides and La^{3+} ion concentration on some properties of Ni–Zn ferrites. *Phys B* 2014; **445**: 60–67.

[38] T.J. Shinde, A.B. Gadkari, P.N. Vasambekar. Magnetic properties and cation distribution study of nanocrystalline Ni–Zn ferrites. *J Magn Magn Mater* 2013; **333**: 152–155

[39] D. Boys, S. Legvold. Thermal conductivities and Lorenz functions of Dy, Er, andLu single crystals. *Phys. Rev* 1968; **174**: 377–384.

[40] W. Nellis, S. Legvold. Thermal conductivities and Lorenz functions of gadolinium, terbium, and holmium single crystals. *Phys Rev* 1969; **180**: 581–590.

[41] B. Zhou, Y. Zhang, C. Liao, C. Yan. Rare-earth-mediated magnetism and magneto-optical Kerr effects in nanocrystalline $CoFeMn_{0.9}RE_{0.1}O_4$ thin films. *J Magn Magn Mater* 2004; **280**: 327–333.

[42] M.L.C.N. Rezlescu, E. Rezlescu, C. Pasnicu. Effect of rare earth ions on some properties of a nickel–zinc ferrite. *J Phys Condens Matter* 1994; **6**: 5716-5723.

[43] A.C.F.M. Costa, E. Tortella, M.R. Morelli, R.H.G.A. Kiminami. Synthesis, microstructure and magnetic properties of Ni–Zn ferrites. *J Magn Magn Mater* 2003; **256**: 174–182.

[44] T. Tsutaoka. Frequency dispersion of complex permeability in Mn–Zn and Ni–Zn spinel ferrites and their composite materials. *J Appl Phys* 2003; **93**: 2789–2796.

[45] M.A. Gabal. Effect of Mg substitution on the magnetic properties of NiCuZn ferrite nanoparticles prepared through a novel method using egg white. *J Magn Magn Mater* 2009; **321**: 3144–3148.

[46] K. Maaz, S. Karim, A. Mumtaz, S.K. Hasanain, J. Liu, J.L. Duan. Synthesis and magnetic characterization of nickel ferrite nanoparticles prepared by coprecipitation route. *J Magn Magn Mater* 2009; **321**: 1838–1842

[47] M. Younas, M. Atif, M. Nadeem, M. Siddique, M. Idrees, R. Grossinger. Colossal resistivity with diminished tangent loss in Zn–Ni ferrite nanoparticles. *J Phys D: Appl Phys* 2011; **44**: 345402

[48] I.Z. Rahman, T.T. Ahmed. A study on Cu substituted chemically processed Ni–Zn–Cu ferrites. *J Magn Magn Mater* 2005; **290–291**: 1576–1579

[49] V. Šepelák, U. Steinike, D.C. Uecker, S. Wißmann, K.D. Becker. Structural disorder in mechanosynthesized zinc ferrite. *J Solid State Chem* 1998; **135**: 52–58.

[50] C. Caizer, M. Stefanescu. Nanocrystallite size effect on σ_s and Hc in nanoparticle assemblies. *Phys B: Condens. Matter* 2003; **327**: 129–134.

[51] D.L. Mills, A.A. Maradudin. Some thermodynamic properties of a semi-infinite Heisenberg ferromagnetic. *J Phys Chem Solids* 1967, **28**: 1855–1874.

[52] P.V. Hendriksen, S. Linderoth, P.A. Lindgård. Finite-size modifications of the magnetic properties of clusters. *Phys Rev B* 1993; **48**: 7259–7273.

[53] J.P. Chen, C.M. Sorensen, K.J. Klabunde, G.C. Hadjipanayis, E. Devlin, A. Kostikas. Size-dependent magnetic properties of $MnFe_2O_4$ fine particles synthesized by co-precipitation. *Phys Rev B* 1996; **54**: 9288–9296.

[54] E.H. Frei, S. Shtrikman, D. Treves. Critical size and nucleationfield of ideal ferromagnetic particles. *Phys Rev* 1957; **106**: 446–455.